Electrical and Optical Properties of Amorphous SnO$_2$:Ta Films, Prepared by DC and RF Magnetron Sputtering: A Systematic Study of the Influence of the Type of the Reactive Gas

Rainald Mientus [1], Michael Weise [1], Stefan Seeger [1], Rene Heller [2] and Klaus Ellmer [1,*]

[1] Optotransmitter-Umweltschutz-Technologie e.V, Köpenicker Str. 325, 12555 Berlin, Germany; mientus@out-ev.de (R.M.); weise@out-ev.de (M.W.); Seeger@out-ev.de (S.S.)

[2] Helmholtz-Zentrum Dresden-Rossendorf, Institute for Ion Beam Physics and Materials Research, Bautzner Landstr. 400, 01328 Dresden, Germany; r.heller@hzdr.de

* Correspondence: ellmer@out-ev.de

Abstract: By reactive magnetron sputtering from a ceramic SnO$_2$:Ta target onto unheated substrates, X-ray amorphous SnO:Ta films were prepared in gas mixtures of Ar/O$_2$(N$_2$O, H$_2$O). The process windows, where the films exhibit the lowest resistivity values, were investigated as a function of the partial pressure of the reactive gases O$_2$, N$_2$O and H$_2$O. We found that all three gases lead to the same minimum resistivity, while the width of the process window is broadest for the reactive gas H$_2$O. While the amorphous films were remarkably conductive ($\rho \approx 5 \times 10^{-3}$ Ωcm), the films crystallized by annealing at 500 °C exhibit higher resistivities due to grain boundary limited conduction. For larger film thicknesses (d $\gtrsim$ 150 nm), crystallization occurs already during the deposition, caused by the substrate temperature increase due to the energy influx from the condensing film species and from the plasma (ions, electrons), leading to higher resistivities of these films. The best amorphous SnO$_2$:Ta films had a resistivity of lower than 4×10^{-3} Ωcm, with a carrier concentration of 1.1×10^{20} cm^{-3}, and a Hall mobility of 16 cm^2/Vs. The sheet resistance was about 400 Ω/$\square$ for 100 nm films and 80 Ω/$\square$ for 500 nm thick films. The average optical transmittance from 500 to 1000 nm is greater than 76% for 100 nm films, where the films, deposited with H$_2$O as reactive gas, exhibit even a slightly higher transmittance of 80%. These X-ray amorpous SnO$_2$:Ta films can be used as low-temperature prepared transparent and conductive protection layers, for instance, to protect semiconducting photoelectrodes for water splitting, and also, where appropriate, in combination with more conductive TCO films (ITO or ZnO).

Keywords: reactive magnetron sputtering; transparent conductive oxide; electronic transport; doping efficiency; tin dioxide

1. Introduction

Tin dioxide (SnO$_2$) belongs to the class of wide bandgap, oxidic semiconductors that can be, in order to achieve high conductivities, doped up to high carrier concentrations ($> 10^{20}$ cm^{-3}). SnO$_2$, like indium oxide and zinc oxide, also belonging to this material class, exhibits isotropic metal 5s orbitals which form the conduction band of these compound semiconductors. The isotropy of their conduction bands, different from other semiconductors, like silicon or GaAs, is advantageous for the good transport properties (high carrier mobility) of these transparent conductive oxides even in the amorphous state [1,2].

SnO$_2$ is much cheaper than indium oxide, but more expensive than ZnO, the other two widely used transparent conductive oxides (TCO) [3]. An inherent advantage of SnO$_2$ is its high chemical stability [4], making SnO$_2$ suitable for applications in harsh environments, for instance as a transparent and conductive electrode on photoelectrodes for water splitting or as a selectively solar transmitting coating for high-temperature solar thermal applications [5,6].

Highly conductive SnO$_2$ films can be prepared using different deposition methods like spray pyrolysis [7–9], evaporation [10], ion beam sputtering [11], cathode sputtering [12], reactive magnetron sputtering [13], or pulsed laser deposition [14]. Interestingly, SnO$_2$ films, deposited by reactive magnetron sputtering (RMS), exhibit resistivities only in the order of 10^{-3} Ωcm [15,16]. The reason for the only moderate electronic SnO$_2$ film quality when magnetron sputtered, is not clear. Welzel and Ellmer discussed the role of negative oxygen ions in the creation of defects in the growing films. These O$^-$ ions are generated at the negatively charged target surface and accelerated up to high energies (some hundred eV) in the cathode sheath [17]. These high-energetic ions impinge onto the growing film and can create defects, especially oxygen interstitials (O$_i$), that are detrimental to the electronic film quality [18].

The band structure of SnO$_2$ was calculated recently by Schleife et al. [19]. They obtain a direct band gap energy of 3.65 eV, which is in very good agreement with the experimental value E$_g$ = 3.59 eV. The conduction band of SnO$_2$ is derived from Sn 5s states, i.e., the CB is isotropic with a small effective electron mass of about 0.25 m$_e$, which is advantageous for good electron transport in SnO$_2$.

Due to the formation of oxygen vacancies and/or tin interstitials, which act as donors, unintentionally doped SnO$_2$ shows n-type conductivity. DFT calculations prove that oxygen vacancies in SnO$_2$ lead to shallow donor states [20].

By adjusting the oxygen partial pressure during the deposition, resistivity values as low as some 10^{-3} Ωcm were achieved by reactive magnetron sputtering at low substrate temperatures. However, these resistivity values are not stable under normal environmental conditions or when annealed in oxygen-containing atmospheres, caused by the reoxidation of the intrinsic defects, reducing the carrier concentration. Thus, in order to achieve high conductivities, SnO$_2$ has to be doped like the other TCO materials (see, for instance, [21–24]). The doping can be done by replacing cations (Sn) by group V elements (P, As, Sb, Bi) or by replacing anions (O) by group VII elements (F, Cl, Br, I). Mostly, antimony (Sb) and chlorine (Cl) or fluorine (F) were used for the preparation of highly conductive SnO$_2$ films [25–28]. The SnO$_2$:Cl(F) films, especially, were deposited by atmospheric pressure chemical vapour deposition (APCVD), also named spray pyrolysis, at quite high temperatures in the range of 400 to 600 °C.

SnO$_2$, deposited at such high temperatures, exhibit good electronic and optical properties, however, such high temperatures cannot be used for all applications, for instance, for films on temperature-sensitive substrates (plastic), or in case of the deposition of SnO$_2$ films onto active devices, like thin film solar cells or photoelectrodes. In these cases, low-temperature deposition processes are required, for instance reactive magnetron sputtering [29,30].

Recently, transition metals (V, Nb, Ta) have been investigated as dopants in SnO$_2$. Tantalum (Ta) as a dopant in SnO$_2$ was investigated by Kim et al., who deposited epitaxial SnO$_2$:Ta films on sapphire (Al$_2$O$_3$) by metalorganic chemical vapor deposition (MOCVD) at substrate temperatures between 400 and 600 °C [31]. They reported a minimum resistivity of about 3×10^{-4} Ωcm at a Ta content of 1.5 at%. Toyosaki et al. also prepared epitaxial SnO$_2$:Ta films by pulsed laser deposition (PLD) onto single-crystalline TiO$_2$ (rutile) substrates [32]. They reported a minimum resistivity of 1.1×10^{-4} Ωcm at a Ta content of 5 at% for the SnO$_2$:Ta films, deposited at 800 °C. The use of single-crystalline substrates and the high growth temperatures prohibit these approaches for the large-area deposition of cheap SnO$_2$:Ta films. Nakao et al. tried to overcome some of these limitations by depositing SnO$_2$:Ta films onto glass substrates which have been coated with a 10 nm-thin TiO$_2$ seed-layer [33]. After the deposition onto unheated substrates, these amorphous films were annealed in situ at 600 °C to achieve resistivities as low as 1.9×10^{-3} Ωcm. Weidner et al. recently compared the two dopants antimony

and tantalum in SnO_2 films deposited by magnetron sputtering [34]. They achieved a significantly lower resistivity of SnO_2:Ta (5.4×10^{-4} Ωcm) compared to SnO_2:Sb films by a factor of 3.

SnO_2 films, deposited at low temperatures, are typically X-ray amorphous [35,36]. Amorphous oxide films exhibit the advantage of the absence of grain boundary effects on the electrical transport [1]. Such amorphous oxide films in the In-Ga-Zn-O system with low carrier concentrations have been used successfully for the preparation of transparent and flexible field effect transistors, where the absence of grain boundaries in the channel regions increased the field effect mobility significantly [37]. Recently, indium oxide films were investigated in detail with respect to the relation between structural and electronic transport properties [38]. Buchholz et al. analyzed the transition from amorphous to crystalline In_2O_3 films both experimentally and theoretically.

Another beneficial effect of the absence of grain boundaries in amorphous films is that amorphous films typically exhibit lower diffusion coefficients. This property of amorphous films can be exploited for use in protective films [39].

In this article, the deposition of X-ray amorphous, Ta-doped SnO_2 films prepared by reactive magnetron sputtering from a ceramic target is investigated systematically. The depositions were performed onto unheated glass substrates in order to explore the possibility of depositing these SnO_2 films onto temperature-sensitive substrates (plastics) or sensitive underlying films or devices (thin film solar cells or photoelectrodes for water splitting). We investigated in detail the effects of the plasma excitation (DC or RF, 13.56 MHz) and the type of the reactive gas (O_2, H_2O, N_2O) on the electrical properties of the SnO_2:Ta films. Due to its superior chemical stability, such SnO_2:Ta films are intended for applications as transparent and conductive protection layers [39].

2. Experimental

The SnO_2:Ta films were prepared at different substrate temperatures by reactive magnetron sputtering from a ceramic target in a Leybold Z400 sputtering system, equipped with a fast load-lock. The base pressure of the system is about 5×10^{-4} Pa. While the reactive gases O_2 and N_2O were fed into the sputtering chamber in the conventional way with mass flow controllers (MFC) from gas bottles, the water vapour (p_{H2O} = 23 hPa at 20 °C) was fed into the chamber by a special low-pressure MFC from the liquid H_2O reservoir, a quartz container held at room temperature.

The ceramic $Sn_{0.98}Ta_{0.02}O_2$ target (purity 4N, supplier: EVOCHEM Advanced Materials GmbH) with 75 mm diameter was bonded on a Cu cooling well. It was sintered under reducing conditions, thus also allowing DC plasma excitation. The depositions were done at a target-to-substrate distance of 55 mm onto stationary substrates. Before the deposition, a substrate pretreatment with an RF argon plasma was performed for 1 min (p_{Ar} = 1.8 Pa, P_{RF} = 100 W, $V_{DC} \approx$ 1000 V). The substrate holder could be heated by a resistance heater up to glass substrate temperatures of about 400 °C, measured with a thermocouple.

The film thickness was measured using a DEKTAK profilometer. The optical parameters were obtained by spectroscopic ellipsometry in the photon energy range from 1.5 to 4.2 eV (SE 850, Sentech GmbH, Berlin, Germany). These spectra were fitted and analysed with the commercial optical analysis program 'SpectraRay3' from Sentech. The optical transmittance (*T*) and reflectance (*R*) spectra were measured with an UV/Vis double-beam spectrometer (Cary 05E, Varian) in the spectral range from 200 to 3200 nm (6.2 to 0.38 eV).

The structural properties of the SnO_2:Ta films were analyzed by X-ray diffraction (XRD) with a silicon-stripe detector (D2 Phaser with a Cu-anode and a Lynxeye detector, Bruker AXS) in Bragg–Brentano geometry. The diffraction peaks were fitted by double peaks with Lorentzian peak-shape, thus yielding the positions and widths of the two CuK_α peaks.

The thickness-averaged elemental composition was measured using Rutherford backscattering spectrometry (RBS) on samples deposited onto glassy carbon substrates. He ions with an energy of 1.7 MeV at normal incidence were used for the analysis. Typically, a $^4He^+$ charge of 10 μC was used to collect RBS spectra with good counting statistics. The RBS spectra were simulated with the

software SIMNRA [40]. In order to determine the electron concentration and the Hall mobility, Hall and conductivity measurements were performed with a home-built setup at room temperature at a magnetic flux of 0.74 T. The 10×10 mm^2 samples were contacted in the corners in the van der Pauw geometry. The radial profiles of the electrical parameters were measured in order to investigate the role of negative oxygen ion bombardment which is radially inhomogeneous [41].

The cross-section of the SnO$_2$:Ta films was prepared with Argon ion beam polishing and investigated with transmission electron microscopy (TEM Zeiss LIBRA 200FE) in the bright-field mode including diffraction contrast and zero-energy-loss filtering.

Post-annealing treatments were carried out with an IR-lamp heater (maximum intensity at a wavelength of about 1.5 μm) in vacuum (p = 1×10^{-2} Pa) or in hydrogen atmosphere (p$_{H2}$ = 200 hPa) at a temperature of T = 500 °C. Prior to the annealing, the vacuum chamber was evacuated to a vacuum pressure of about 1×10^{-4} Pa. The heating rate was about 2 K/s and the time at the set temperature was about 2 min.

3. Results and Discussion

3.1. Deposition Characteristics

Figure 1a shows the deposition rate as a function of the discharge power for DC and RF (13.56 MHz) plasma excitation. For both discharge modes, the rate increases linearly with the discharge power, as expected [30], and is independent of the type of the reactive gas (O$_2$, N$_2$O, H$_2$O). While the linear fit curves start at the origin of the x axis for DC excitation, the RF power where the deposition rate is larger than zero is shifted to a value of about 20 W$_{RF}$. This is caused by the fact that the discharge voltages (i.e., the target voltages) are much lower for RF plasma excitation compared to the DC discharge [30]. For RF powers lower than 20 W, the target voltage is lower than the sputtering threshold voltage [42]; thus, no deposition can take place. The deposition rates for RF sputtering are much lower compared to the DC deposition rates; the slopes of the linear rate(power) curves in Figure 1a are 0.24 and 0.66 nm/(min·W) for RF and DC excitation, respectively. This is caused by two effects:

- The lower discharge voltages leading to lower sputtering yields;
- The fact that, in the RF case, the target is only at a sufficiently high negative potential every second half-wave, allowing an acceleration of positive Ar ions to the target surface [43].

Figure 1b displays the partial pressures of the reactive gases O$_2$, N$_2$O, H$_2$O, where the deposited films exhibit the resistivity minimum as a function of the discharge power. It can be seen that more reactive gas is needed with increasing discharge power, i.e., increasing deposition rate. This can be explained by the fact that a certain amount of (reactive) oxygen per deposited amount of metal atoms is needed to prepare highly conductive SnO$_2$:Ta films. This behaviour is also known for other TCO materials, for instance, for ZnO [44]. The amount of reactive gas needed to prepare highly conductive films depends strongly on the type of reactive gas, of the mode of plasma excitation and the deposition temperature. This is due to the different amounts of oxygen, supplied by the different reactive gases. Oxygen gas itself contains the highest relative amount of oxygen compared to N$_2$O and H$_2$O; thus, the lowest partial pressure is needed for pure O$_2$. Although the molecules N$_2$O and H$_2$O contain the same relative amount of oxygen (one third), there is still a difference for both reactive gases which can be explained by the different chemical action of nitrogen (N$_2$O) and hydrogen (H$_2$O): while nitrogen is almost nonreactive, hydrogen is reducing the growing film. Therefore, in case of H$_2$O as reactive gas, a higher amount of oxygen is needed in order to have the same oxidizing effect as N$_2$O. One also has to take into account that the dissociation energies of the stable molecules O$_2$ and H$_2$O ($\approx$5.1 eV [45]) are much higher in comparison to the metastable N$_2$O molecule (E$_{dis}$ $\approx$ 1.6 eV [46]) which shifts the resistivity minimum for N$_2$O nearer to that of O$_2$.

This is clearly visible if the necessary reactive gas partial pressure is plotted versus the deposition rate, as shown in Figure 1c. Besides the effects of the reactivity and composition of the reactive

gas, the effect of the different degrees of gas dissociation in a DC and an RF discharge can also be derived from Figure 1c. For the case of DC plasma excitation, the films were deposited both at room temperature as well as at a substate temperature of 400 °C. Obviously, the reactivity of the gas (O_2 in this case) is significantly improved at a higher substrate temperature, thus a lower oxygen partial pressure is required at a higher deposition temperature.
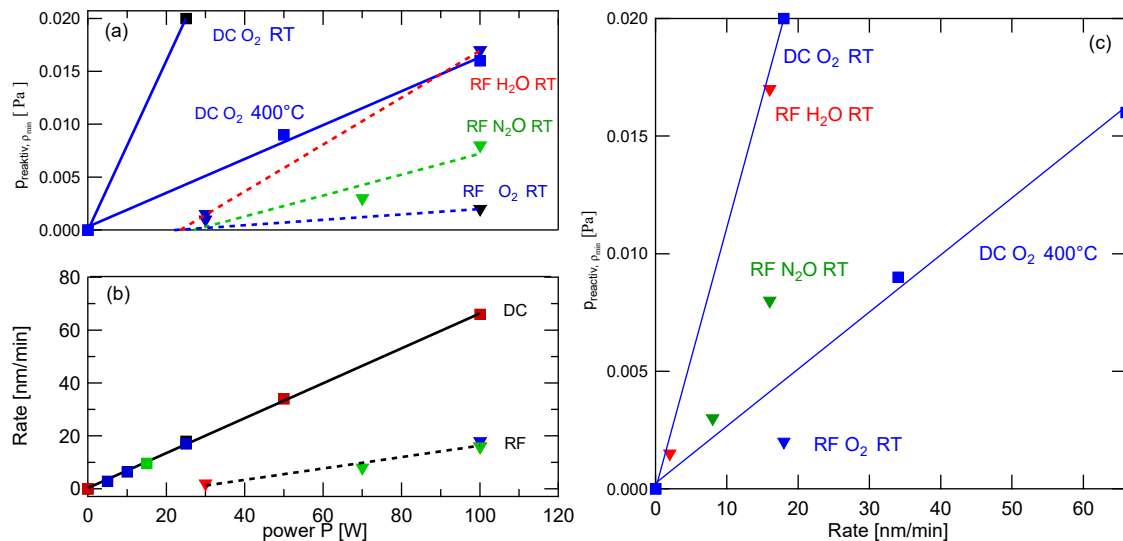

Figure 1. (**a**) Partial pressures of the reactive gases where the resistivity minimum was found as a function of the discharge power. (**b**) Deposition rate as a function of the discharge power for DC and RF (13.56 MHz) plasma excitation. Reactive gases used were O_2, H_2O and N_2O. (**c**) Partial pressures of the reactive gases where the resistivity minimum was found as a function of the deposition rate. Deposition parameters: p_{total} = 0.5 Pa; square/ triangular symbols: DC/RF excitation; reactive gases: O_2 (blue), N_2O (green), H_2O (red); black fit lines: room temperature deposition (RT), red fit lines: 400 °C deposition.

3.2. Phase Composition

The XRD patterns of the as-deposited films, displayed in Figure 2, exhibit no diffraction peaks; this means that these films are X-ray amorphous at film thicknesses below about 200 nm. While thicker films (≈500 nm) deposited by DC magnetron sputtering are still X-ray amorphous, the thicker films, prepared by RF magntron sputtering, exhibit X-ray peaks, corresponding to the tetragonal (rutile-like) structure of cassiterite (SnO_2) (powder diffraction file PDF®_01_070_4175, The International Centre for Diffraction Data, Newton Square, USA).

While the X-ray amorphous DC-sputtered films had a constant resistivity of about 5×10^{-3} Ωcm, the films which started to crystallize at larger thicknesses showed an increased resistivity for a thickness of about 500 nm (see below). The Raman spectra (not displayed here) of as-deposited SnO_2:Ta films show only weak, broad features ascribed to the glass substrates. Since Raman spectroscopy is able to detect structural features/phases for crystallite sizes in the few nm range, i.e., smaller than is possible by XRD, we conclude that the SnO_2:Ta films are really amorphous.
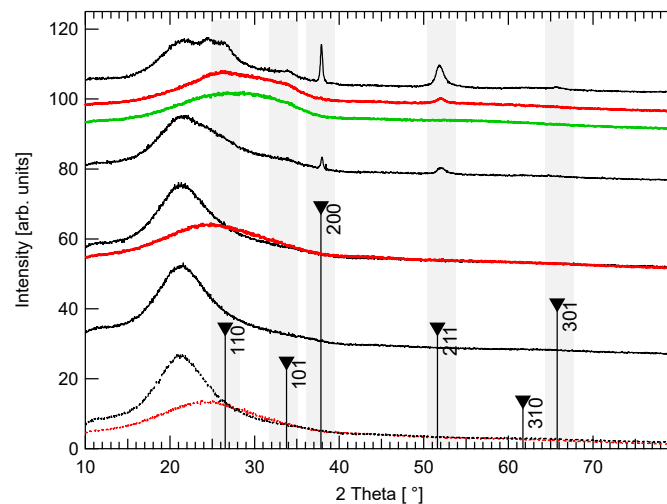
Figure 2. XRD patterns of SnO$_2$:Ta films deposited by RF (thin, black lines) and DC (thick, red and green lines) magnetron sputtering in Ar+O$_2$ atmosphere for different durations. Deposition parameters: RF: P = 100 W, p = 0.5 Pa, t = 2, 5, 13 and 23 min (from the bottom); DC: P = 25 W, p = 0.5 Pa, t = 5 and 28 min. Film thicknesses increase from about 40 to 450 (500, DC) nm with increasing deposition time. Thick, DC-sputtered films were deposited without (red curve) and with (green curve) three pauses. For comparison, the XRD patterns for the bare substrates quartz (Suprasil, black) and borosilicate glass (D263T, red) are plotted as dotted lines at the bottom. The bars at the bottom of the figure display the diffraction pattern according to the powder diffraction file PDF®_01_070_4175 for SnO$_2$-cassiterite (The International Centre for Diffraction Data, Newton Square, USA).

3.3. Resistivity

The reactive gas partial pressure dependence of the resistivity, the carrier concentration and the Hall mobility of the SnO$_2$:Ta films are displayed in Figure 3. While the discharge voltage and the deposition rate are nearly constant in the investigated partial pressure range, the resistivity exhibits a strong decrease with increasing oxygen partial pressure. A resistivity minimum is found at an oxygen partial pressure of about 2×10^{-2} Pa; further increasing the O$_2$ partial pressure leads to a slight increase in the resistivity.
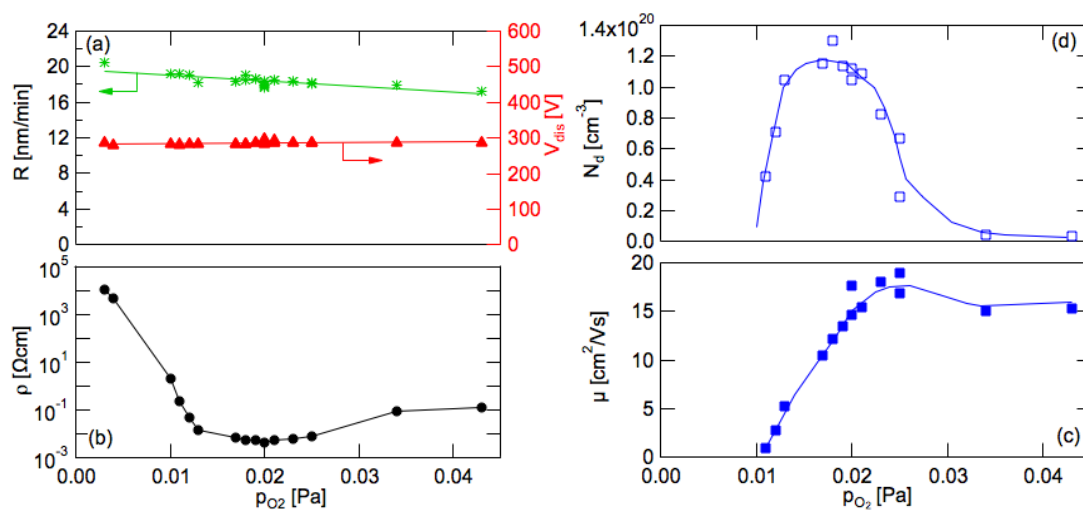

Figure 3. (**a**) Deposition rate (green) and discharge voltage (red), (**b**) resistivity (**c**) mobility and (**d**) carrier concentration as a function of the reactive gas partial pressure. Deposition parameters: P$_{DC}$ = 25 W, p$_{total}$ = 0.5 Pa, reactive gas: O$_2$, RT deposition. The lines in (**a**) are linear fit curves, while the lines in (**b–d**) are thought of as guides to the eye.

The resistivity minimum comes about by a local maximum of the carrier concentration and a maximum Hall mobility at the oxygen partial pressure where the minimum resistivity is obtained.

The effects of the different plasma excitation modes (DC or RF, 13.56 MHz) on film resistivity are shown in Figure 4a. It can be seen that at the same deposition rate, realized by different discharge powers for DC (25 W) and RF excitation (100 W), the O_2-partial pressure where the minimum resistivity is obtained is significantly lower for RF-, compared to DC-excitation. This, we ascribe to the much higher density of reactive oxygen species (O, O*, O^+) in the RF discharge, which was measured already in 1998 by us for the reactive magnetron sputter deposition of ZnO:Al films [47]. The minimum resistivity is about the same for both excitation modes ($\rho_{min} \approx 5 \times 10^{-3}$ Ωcm); however, the width of the minimum is significantly wider in case of DC plasma excitation.
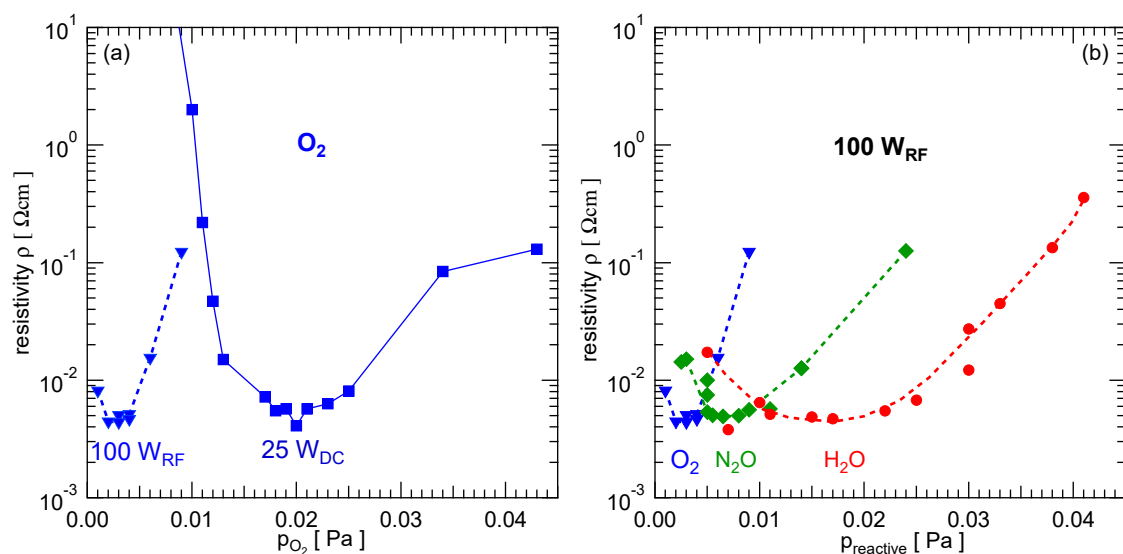

Figure 4. (**a**) Partial pressure dependence of the resistivity for the reactive gas O_2 for DC and RF plasma excitation. The deposition rate is the same in both cases (R $\approx$ 18 nm/s). (**b**) Dependence of the resistivity on the partial pressure of the reactive gases O_2, N_2O and H_2O for RF plasma excitation. Deposition parameters: P_{DC} = 25 W, P_{RF} = 100 W, p_{total} = 0.5 Pa, RT deposition.

Figure 4b shows the reactive gas partial pressure dependence of the resistivity for the three reactive (oxygen-containing) gases O_2, N_2O and H_2O. For all three gases, a resistivity minimum exists with nearly the same value. The position and the width of the $\rho(p_{reactive})$ curves are clearly different for the three oxygen-containing reactive gases. This is plausible, taking into account the different molar concentrations of oxygen in the different molecules—see also Section 3.1. Using H_2O as a reactive gas, the resistivity minimum occurs at the highest partial pressure, although H_2O contains the same relative amount of oxygen as N_2O. This can be explained by the reductive effect of hydrogen, thus requiring a higher partial pressure to have the same oxidizing effect, as in the case of N_2O. An advantage of H_2O as reactive gas is the wider resistivity minimum, making it easier to adjust the reactive gas partial pressure.

In order to analyze the carrier transport process, the Hall mobility is displayed as a function of the carrier concentration, see Figure 5a−c. It can be seen that, independently of the used reactive gases, the mobility first increases steeply with increasing reactive gas partial pressure, reaching maximum values of about 15–20 cm^2/Vs at carrier concentrations of about 1×10^{20} cm^{-3}. The strong increase in the electron mobility with increasing reactive gas partial pressure at a nearly constant carrier concentration (see the arrows in Figure 5) can be tentatively explained by a higher defect density (Sn or SnO inclusions) at low reactive gas partial pressure. These defects act as scattering centers, thus reducing the carrier mobility. A theory for the explanation of this steep $\mu(N)$ dependence has yet to be developed.
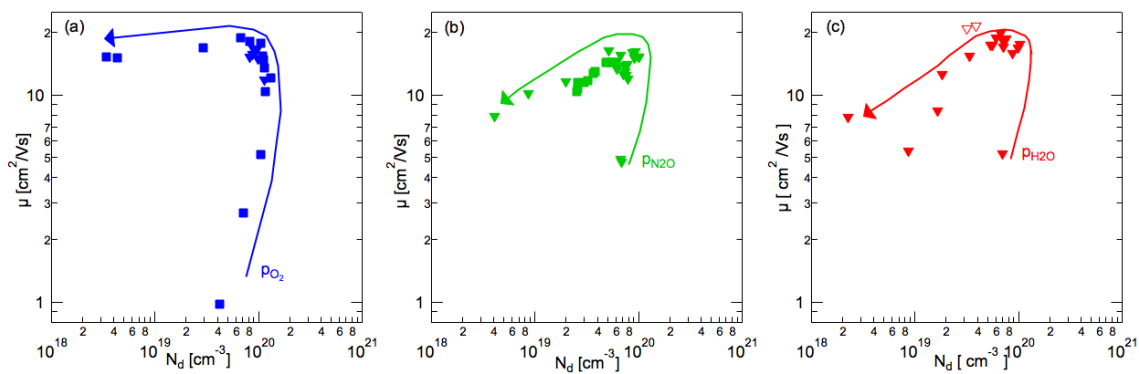
Figure 5. Dependence of the Hall electron mobility on the carrier concentration for SnO_2:Ta films sputtered with different reactive gases: (**a**) O_2 (blue) (**b**) N_2O (green), and (**c**) H_2O (red). The lines with arrows in the figures indicate the increasing reactive gas partial pressure. Deposition parameters: ■ 15 W_{DC}, ■ 25 W_{DC}, ▼ ▼ ▼ 100 W_{RF}, ▽ 30 W_{RF}, p_{total} = 0.5 Pa, RT.

Further increasing $p_{reactive}$ leads to a gradually decreasing mobility, less for O_2, and stronger for N_2O and H_2O. The carrier concentration decreases much more, by nearly two orders of magnitude. This behaviour is similar to that of other amorphous semiconducting oxide films, for instance, $InGaZnO_4$ [37,48]. According to Nomura et al., the electronic transport in these amorphous oxides is governed by a percolation conduction over a distribution of potential barriers at the conduction band edge. Other than in single- or polycrystalline semiconductors, the band edges are no longer straight over larger volumes of material, i.e., the amorphous oxides exhibit small potential barriers on the nanoscale, caused by the randomness of the amorphous material in general and by the random distribution of defects (Ta_{Sn}, O_i, V_O etc.) especially.

The maximum carrier concentration is relatively low, compared to other TCO materials (ITO, ZnO). Taking into account the concentration of Ta in the SnO_2:Ta films (Ta/Sn ≈ 0.5 at%), the electrical activation of Ta, assuming that Ta on tin lattice sites (Ta_{Sn}) acts as a donor, is quite low, in the order of 22%, using the molecular number density of SnO_2 of 3.125×10^{22} molecules/cm^3 and the maximum carrier concentration of about 1.2×10^{20} cm^{-3}. The quite low carrier concentrations of the SnO_2:Ta films could be caused by an inactivation/compensation of the donors (Ta_{Sn}) by other defects, already mentioned above (O_i, V_O etc.). Similar compensation effects were recently reported by T-Thienprasert et al. and by us for Al-doped ZnO [49,50].

3.4. Film Composition (RBS)

The film composition was determined by Rutherford back-scattering analysis (RBS). To this purpose, the SnO_2:Ta films were deposited onto glassy carbon (Sigradur) substrates which produce, due to the low atom mass of carbon, a very low background for the backscattering peaks of oxygen, tin and tantalum, thus allowing an exact determination of the average film composition [51].

Typical RBS spectra of two SnO_2:Ta films on logarithmic scale are shown in Figure 6a. Besides the edge of the carbon substrate, the peaks for O, Sn and the shoulder for the dopant Ta are clearly visible. At channel numbers around 600, a small peak is visible that belongs to argon. It is caused by two effects:

(i)   Ar is implanted into the glassy carbon during the surface cleaning of the substrates by the Ar-RF plasma treatment (narrow peak at channel 590);

(ii) Ar is included (buried) into the growing film during the deposition of the SnO_2:Ta film. This is caused both by the continuous coverage of the film surface by neutral argon atoms from the sputtering atmosphere as well as the bombardment of the film surface by energetic Ar ions, atoms and metastable atoms [52,53] which are then covered by the film atoms.
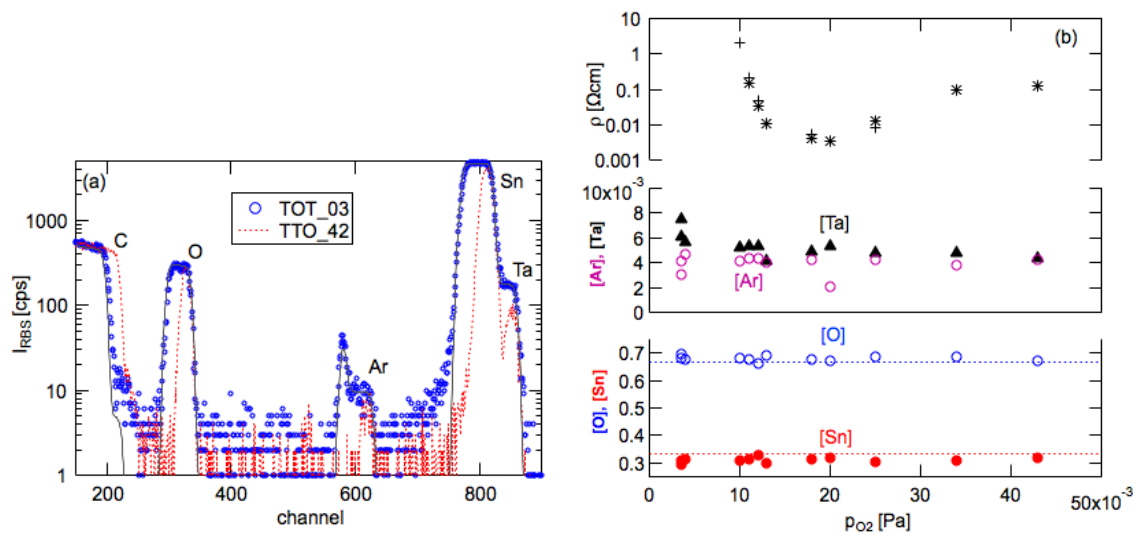
Figure 6. (**a**) Rutherford backscattering spectra of two SnO_2:Ta films on a logarithmic intensity scale displaying the backscattering peaks/shoulders for the elements Ta, Sn, Ar, O and C (with decreasing energy, i.e., channel number). The two films were deposited at low- (TOT_03) and high- (TTO_42) oxygen partial pressures. The thin line is the simulated Rutherford backscattering spectrometry (RBS) curve of the film TOT_03. (**b**) Average chemical composition as a function of the reactive gas pressure in comparison to the resistivity of the films.

The concentration of argon in the films is about 0.4 at% for films deposited at room temperature. For the SnO_2:Ta films deposited at a high temperature (400 °C), the Ar content is much lower (≈ 0.1 at%), caused by the higher desorption of the Ar atoms during the film growth [54,55].

By integrating the peaks for O, Sn and Ta, the average composition of the films was determined, displayed in Figure 6b as a function of the oxygen partial pressure. It is clearly visible that the dopant (Ta) concentration does not depend on the reactive gas partial pressure and the type of gas. It is nearly constant at a concentration of 1.5 at%. This means that the observed variation in the electrical parameters as a function of the reactive gas pressure is not caused by a variation in the chemical dopant amount, but by a varying electrical activation of the dopant Ta and/or by compensation of the electrons by acceptor-like defects—see, for instance, [49,50].

The oxygen-to-metal ratio is almost constant within a measurement accuracy of about ≈ 2 at%. Since we observe a strong variation in the electrical parameters when varying the reactive gas partial pressure, this has to be caused by an oxygen concentration variation which cannot be detected by RBS.

3.5. Thickness Dependence

Most of the deposited SnO_2:Ta films had thicknesses of about 100 nm. For applications where low sheet resistances are needed, thicker films have to be deposited. Therefore, the thickness dependence of the electrical film properties was investigated. Figure 7a shows the dependence of deposition rate, resistivity, carrier concentration and Hall mobility on the film thickness up to about 450 nm. As expected, the deposition rate is constant. In contrast to what is known for other TCO materials (see Figure 7b, [56]), the resistivity increases significantly with increasing film thickness, caused mainly by the decrease in the carrier concentration. A similar behaviour was observed by Minami et al. and by Brousseau et al. for undoped SnO_2 films, also deposited by RF magnetron sputtering [57,58].
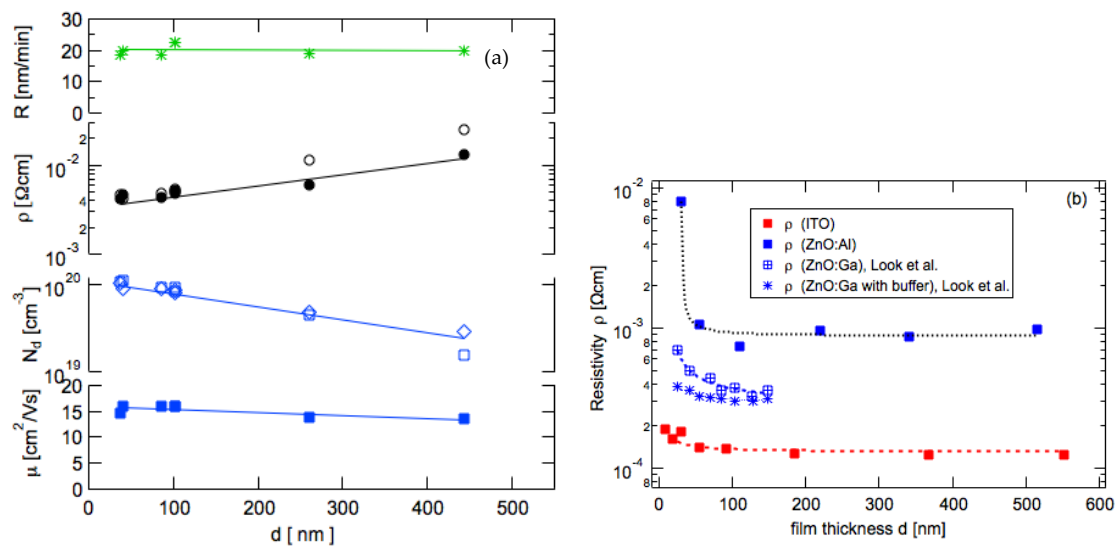
Figure 7. (**a**) Thickness dependence of the deposition rate and the electrical parameters of SnO_2:Ta films. Deposition parameters: P_{RF} = 100W, p = 0.5Pa, RT, O_2. (**b**) Thickness dependence of the resistivity of ZnO:Al and ITO films, taken from reference [56].

The well-known behaviour of a decreasing resistivity with increasing film thickness can be explained by an increasing grain size and the decreasing effect of surface and interface carrier scattering, described by the Fuchs–Sondheimer theory, see [56,59,60].

To explain the contrary behaviour of our SnO_2:Ta films, one has to take into account that the films with larger film thicknesses (> 200 nm) are no longer X-ray amorphous, i.e., these films are, at least partly, polycrystalline with grain boundaries.

Figure 8 shows a TEM cross-sectional picture of a 500 nm thick SnO_2:Ta film, deposited by RF magnetron sputtering. It can clearly be seen that the film is composed of an amorphous part, directly grown on the glass substrate. After a certain thickness is reached, varying locally, a spontaneous crystallization sets in and the SnO_2:Ta growth is transformed to polycrystalline growth. A similar behaviour was observed by us earlier for the growth of indium–tin oxide (ITO) films by reactive magnetron sputtering from a metallic InSn10wt% target [61]. In this case, the films were deposited onto intentionally unheated substrates and the increase in the substrate temperature occurred during the film growth.
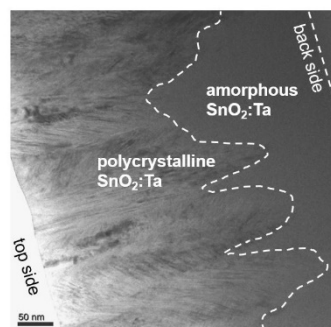

Figure 8. Cross-sectional transmission electron micrograph of a ≈ 500 nm thick SnO_2:Ta film. The flat interface to the glass substrate and the corrugated interface between the amorphous (bottom) and the polycrystalline (top) parts of the film are marked by dashed lines. The image was taken in the bright field modus, including diffraction contrast and zero-energy-loss filtering. Deposition parameters: P_{RF} = 100W, p = 0.5Pa, RT, Ar+N_2O.

The crystallization of the thicker SnO_2:Ta films is due to the increasing substrate temperature during the deposition, caused by the total energy flux to the growing film [62,63]. Based on the

measured energy flux, it is estimated that the substrate temperature reaches values > 100 °C. That the increased substrate temperature causes the film crystallization was proven by depositing some films stepwise, making a pause for cooling down every 100 nm. Thick films (500 nm) deposited in this way were X-ray amophous and had resistivity values comparable to thin films.

3.6. Radial Profiles

The radial profiles of the electrical film properties were analyzed for DC and RF plasma excitation. Such profiles are an important aspect for magnetron sputtering deposition onto a stationary substrate, since the plasma/ion assistance of the film growth varies radially significantly, caused by the plasma torus which is formed in front of the target [18]. For the deposition of TCO films it is often reported that radial profiles of the resistivity exhibit pronounced maxima or minima opposite the erosion groove of the target which are formed due to the torus-like shape of the magnetron plasma—see, for instance, [18,64–66].

Figure 9 displays the radial distributions of the electrical parameters and the film thickness for DC and RF plasma excitation. While the radial thickness distributions for both excitation modes are almost the same, exhibiting the expected bell-shaped curve, the resistivity distributions in the as-deposited state are clearly different for DC and RF plasma excitation. While the resistivity of the RF-deposited films is only slightly varying over the diameter of the substrate, the resistivity distribution of the DC-deposited films shows a significant increase in ρ towards the border of the substrate by a factor of about 3. The regions, where the resistivity is high, coincide with the radial position of the erosion groove of the target. This points to the effect of a high-energetic negative ion bombardment of the growing film, as discussed recently by us [17,18].
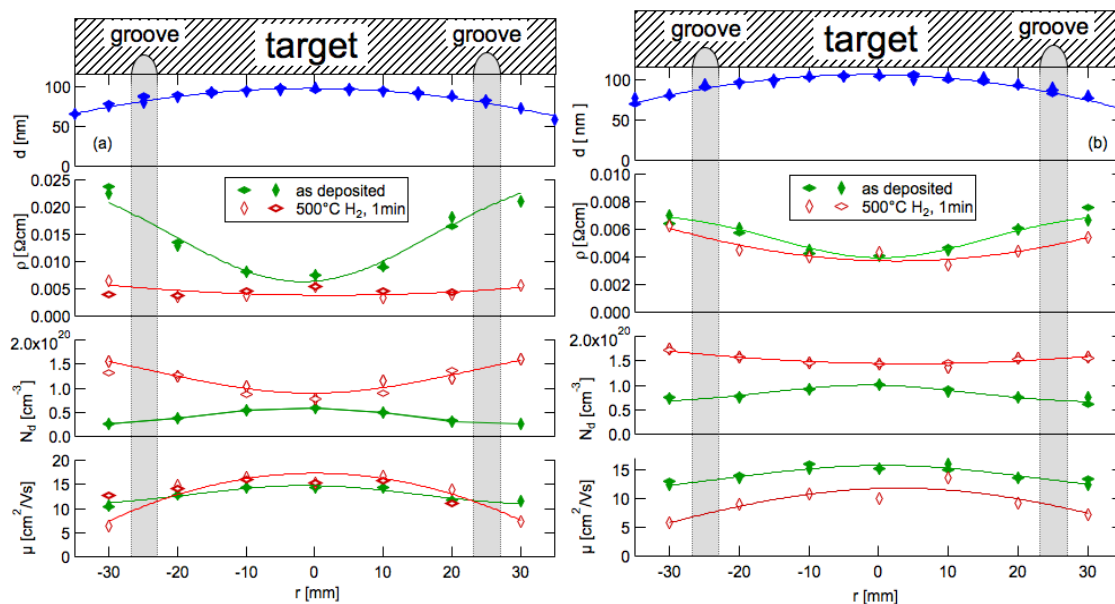

Figure 9. Radial profiles of film thickness, resitivity, carrier concentration and Hall mobility for (**a**) DC plasma excitation (P_{DC} = 15 W, V_T = 317V, 0.5Pa, RT, N_2O, R = 10 nm/min) and (**b**) RF plasma excitation (P_{RF} = 100 W, V_T = 92 V, 0.5Pa, RT, N_2O, R = 17 nm/min.). Vertically and horizontally elongated diamonds mark datapoints measured over two diameters in the substrate plane, perpendicular to each other. The red symbols and curves display the electrical parameters after annealing at 500 °C in H_2 for 1 min. The lines are Gaussian fits to the datapoints.

It has become known in recent years that, in sputtering processes with electronegative elements (for instance O, F, Cl, S, Se, but also Au, Pt, Ag, Sn, Bi—see reference [67] for the electron affinity values) negative ions are accelerated away from the negatively biased target surface towards the substrate, i.e., the growing film. Due to the high discharge/target voltages, even in the modern magnetron sputtering

systems, the energies of these negative ions are in the range of some 100 eV, which therefore leads to the generation of defects in the growing film. In the beginning of the sputtering technology, before the invention of the magnetron sputtering sources, the discharge voltages were much higher (some kV) which led to a very high-energy bombardment of the growing films, sometimes ending up not in film deposition but in film and substrate etching [68]. Short-term post-anneling of the SnO_2:Ta films at 500 °C in the hydrogen atmosphere of the dc-sputtered films reduces their resistivities even in the region opposite the target groove, while the resistivity of rf-sputtered films was nearly unaffected.

3.7. Transmittance and Reflectance

The transmittance and reflectance spectra of SnO_2:Ta films are shown exemplarily in Figure 10a,b. With increasing N_2O partial pressure, the amount of non-oxidized Sn in the films is reduced and the films become more transparent in the visible spectral range. The absorption edge shifts to smaller wavelengths. This means that the optical band gap energy is increased, caused by the Burstein–Moss effect [69,70].
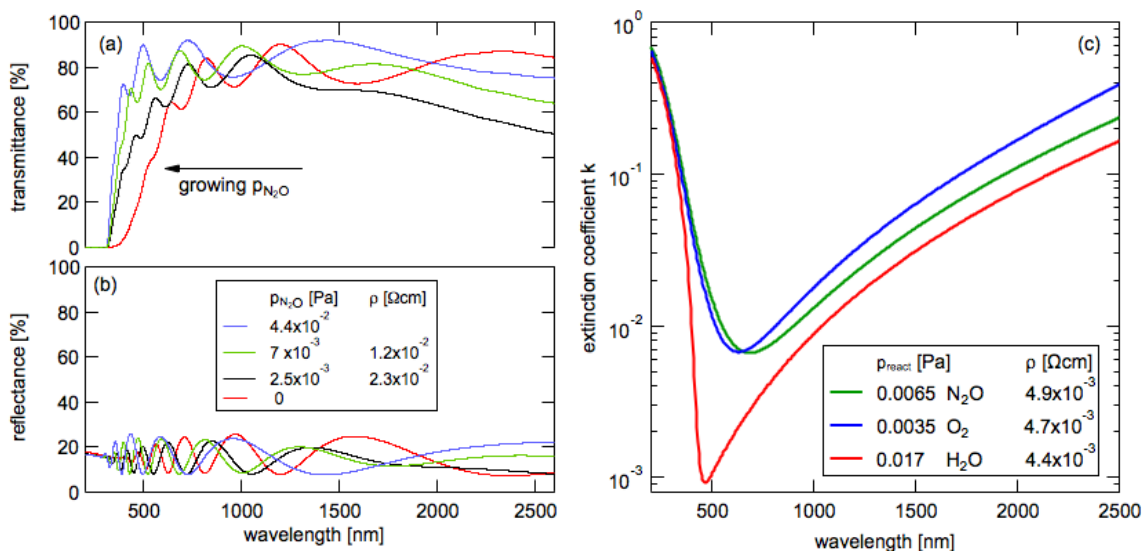

Figure 10. (**a**) Transmittance T and (**b**) reflectance R spectra in the wavelength range from 200 to 2600 nm of SnO_2:Ta films, deposited at different N_2O partial pressures. (**c**) Spectral extinction coefficients of 3 SnO_2:Ta films, deposited with different reactive gases and nearly the same minimum resistivity of about 4.7x10^{-3} Ωcm. Deposition parameters: P_{RF} = 100 W, 0.5Pa, RT.

From the transmittance and reflectance curves (see Figure 10a,b), the optical constants n and k have been calculated. The extinction coefficient k of three SnO_2:Ta films is shown in Figure 10c as a function of the wavelength. These films were prepared with the three reactive gases O, N_2O and H_2O under conditions that yielded minimum resistivities of about 4.7×10^{-3} Ωcm. While the films deposited with O or N_2O exhibit a minimum k value of about 7×10^{-3} in the visible spectral range, the films deposited in Ar+H_2O show a much lower extinction coefficient, lower than 1×10^{-3}. A tentative explanation of this striking effect is the passivation of deep defects in the band gap of the SnO_2:Ta films by the hydrogen from the sputtering atmosphere when using H_2O as a reactive sputtering gas.

4. Conclusions

Conductive and transparent SnO_2:Ta films were prepared at low substrate temperatures (<100 °C) by reactive magnetron sputtering from a ceramic target in various gas mixtures: Ar/O_2(N_2O, H_2O). The width of the process window with respect to the reactive gas partial pressure depends on the type of the reactive gas; it is wider for N_2O and H_2O, mostly due to the dilution of the oxygen content in the

compound gases. The SnO_2:Ta films are X-ray amorphous in the as-deposited state. By heating the films to temperatures above 500 °C, the films start to crystallize, accompanied by an increased resistivity. For RF deposition (larger energy flux to the growing film) at larger film thicknesses (d >≈ 150 nm), i.e., longer deposition times, crystallization occurs during the deposition, caused by the substrate temperature increase due to the energy influx from the condensing film species and the plasma. While the amorphous films are remarkably conductive ($\rho \approx 5 \times 10^{-3}$ Ωcm), the crystallized films exhibit higher resistivities due to grain-boundary-limited conduction. The best amorphous SnO_2:Ta films had a resistivity of better than 4×10^{-3} Ωcm with a carrier concentration of 1.1×10^{20} cm^{-3}, and a Hall mobility of 16 cm^2/Vs. The sheet resistance was about 400 Ω/□ for 100 nm films and 80 Ω/□ for 500 nm thick films. The average optical transmittance from 500 to 1000 nm is greater than 76% for 100 nm films, where the films, deposited with H_2O as a reactive gas, exhibit a slightly higher transmittance of 80%.

The crystallization of the SnO_2:Ta films is not only detrimental for the electrical transport properties of the films; grain boundaries are also diffusion paths for atoms and molecules in gaseous or liquid environments. Since these films were deposited at low temperatures, they are amorphous, thus improving the resistivity against degradation and etching.

These X-ray amorpous SnO_2:Ta films can be used as low-temperature transparent and conductive protection layers, for instance to protect semiconducting photoelectrodes for water splitting, and also, where appropriate, in combination with more conductive TCO films (ITO or ZnO).

References

1. Hosono, H.; Kikuchi, N.; Ueda, N.; Kawazoe, H. Working hypothesis to explore novel wide band gap electrically conducting amorphous oxides and examples. *J. Non Cryst. Solids* **1996**, *198*, 165–169. [CrossRef]

2. Hosono, H. Recent progress in transparent oxide semiconductors: Materials and device application. *Thin Solid Films* **2007**, *515*, 6000–6014. [CrossRef]

3. Ellmer, K. Past achievements and future challenges in the development of optically transparent electrodes. *Nat. Photonics* **2012**, *6*, 809–817. [CrossRef]

4. Vossen, J.L.; Kern, W. (Eds.) *Thin Film Processes II*; Academic Press: Cambridge, MA, USA, 1991; p. 866.

5. Lungwitz, F.; Escobar-Galindo, R.; Janke, D.; Schumann, E.; Wenisch, R.; Gemming, S.; Krause, M. Transparent conductive tantalum doped tin oxide as selectively solartransmitting coating for high temperature solar thermal applications. *Solar Ener. Mat. Solar Cells* **2019**, *196*, 84–93. [CrossRef]

6. Kavan, L.; Steier, L.; Grätzel, M. Ultrathin Buffer Layers of SnO_2 by Atomic Layer Deposition: Perfect Blocking Function and Thermal Stability. *J. Phys. Chem. C* **2017**, *121*, 342–350. [CrossRef]

7. Fischer, A. Dünne Halbleiterschichten auf Glas. *Z. Naturforsch.* **1954**, *9*, 508–511. [CrossRef]

8. Ishiguro, K.; Sasaki, T.; Arai, T.; Imai, I. Optical and Electrical Properties of Tin Oxide Films. *J. Phys. Soc. Jap.* **1958**, *13*, 296–304. [CrossRef]

9. Shanthi, E.; Banerjee, A.; Dutta, V.; Chopra, K.L. Electrical and Optical Properties of Undoped and Antimony-Doped Tin Oxide Films. *J. Appl. Phys.* **1980**, *51*, 6243–6251. [CrossRef]

10. Spence, W. The uv Absorption Edge of Tin Oxide Thin Films. *J. Appl. Phys.* **1967**, *38*, 3767–3770. [CrossRef]

11. Weissmantel, C.; Fiedler, O.; Hecht, G.; Reisse, G. Ion beam sputtering and its application for the deposition of semiconducting films. *Thin Solid Films* **1972**, *13*, 359–366. [CrossRef]

12. Manifacier, J.C. Thin Metallic Oxides as Transparent Conductors. *Thin Solid Films* **1982**, *90*, 297–308. [CrossRef]

13. Stjerna, B.; Granqvist, C.G.; Seidel, A.; Häggström, L. Characterization of RF-Sputtered SnO$_x$ Thin Fims by Electron Microscopy, Hall-Effect Measurement, and Mössbauer Spectrometry. *J. Appl. Phys.* **1990**, *68*, 6241–6245. [CrossRef]

14. Nakao, S.; Hirose, Y.; Fukumura, T.; Hasegawa, T. Carrier generation mechanism and effect of tantalum-doping in transparent conductive amorphous SnO$_2$ thin films. *Jap. J. Appl. Phys.* **2014**, *53*, 5. [CrossRef]

15. Goodchild, R.G.; Webb, J.B.; Williams, D.F. Electrical Properties of Highly Conducting and Transparent Thin Films of Magnetron Sputtered SnO2. *J. Appl. Phys.* **1985**, *57*, 2308–2310. [CrossRef]

16. *Handbook of Transparent Conductors*; Ginley, D.S.; Hosono, H.; Paine, D.C. (Eds.) Springer: New York, NY, USA, 2010; p. 534.

17. Welzel, T.; Ellmer, K. Negative oxygen ion formation in reactive magnetron sputtering processes for transparent conductive oxides. *J. Vac. Sci. Techn. A* **2012**, *30*, 61306. [CrossRef]

18. Ellmer, K.; Welzel, T. Reactive Magnetron Sputtering of Transparent Conductive Oxide Thin Films: Role of Energetic Particle (Ion) Bombardment. *J. Mat. Res.* **2012**, *27*, 765–779. [CrossRef]

19. Schleife, A.; Varley, J.B.; Fuchs, F.; Rödl, C.; Bechstedt, F.; Rinke, P.; Janotti, A.; Walle, C.G.V.d. Tin dioxide from first principles: Quasiparticle electronic states and optical properties. *Phys. Rev. B* **2011**, *83*, 35116. [CrossRef]

20. Ágoston, P.; Albe, K.; Nieminen, R.M.; Puska, M.J. Intrinsic n-Type Behavior in Transparent Conducting Oxides: A Comparative Hybrid-Functional Study of In$_2$O$_3$, SnO$_2$, and ZnO. *Phys. Rev. Lett.* **2009**, *103*, 245501. [CrossRef]

21. Minami, T. Transparent Conducting Oxide Semiconductors for Transparent Electrodes. *Semicond. Sci. Techn.* **2005**, *20*, S35–S44. [CrossRef]

22. Ellmer, K. Resistivity of Polycrystalline Zinc Oxide Films: Current Status and Physical Limit. *J. Phys. D Appl. Phys.* **2001**, *34*, 3097–3108. [CrossRef]

23. Ellmer, K.; Bikowski, A. Topical Review: Intrinsic and Extrinsic Doping of ZnO and ZnO Alloys. *J. Phys. D* **2016**, *49*, 413002. [CrossRef]

24. Bellingham, J.R.; Phillips, W.A.; Adkins, C.J. Intrinsic Performance Limits in Transparent Conduction Oxides. *J. Mat. Sci. Lett.* **1992**, *11*, 263–265. [CrossRef]

25. Chopra, K.L.; Major, S.; Pandya, D.K. Transparent Conductors- A Status Review. *Thin Solid Films* **1983**, *102*, 1–46. [CrossRef]

26. Hartnagel, H.L.; Dawar, A.L.; Jain, A.K.; Jagadish, C. *Semiconducting Transparent Thin Films*; Institute of Physics Publishing: Bristol, UK, 1995; p. 358.

27. Swallow, J.E.N.; Williamson, B.A.D.; Whittles, T.J.; Birkett, M.; Featherston, T.J.; Peng, N.; Abbott, A.; Farnworth, M.; Cheetham, K.J.; Warren, P.; et al. Self-Compensation in Transparent Conducting F-Doped SnO$_2$. *Adv. Funct. Mater.* **2017**, *28*, 1701900. [CrossRef]

28. Koch, H. Zum optischen Verhalten halbleitender Zinndioxydschichten im nahen Ultrarot bei Zimmertemperatur. *phys. stat. sol.* **1963**, *3*, 1619–1628. [CrossRef]

29. Thornton, J.A. High Rate Sputtering Techniques. *Thin Solid Films* **1981**, *80*, 1–11. [CrossRef]

30. Ellmer, K. Magnetron Discharges for Thin Film Deposition. In *Low Temperature Plasmas. Fundamentals, Technologies and Techniques*; Hippler, R., Kersten, H., Schmidt, M., Schoenbach, K.H., Eds.; Wiley-VCH: Berlin/Heidelberg, Germany, 2008; Volume 2, pp. 675–715.

31. Kim, Y.-W.; Lee, S.W.; Chen, H. Microstructural evolution and electrical property of Ta-doped SnO$_2$ films grown on Al$_2$O$_3$(0001) by metalorganic chemical vapor deposition. *Thin Solid Films* **2002**, *405*, 256–262. [CrossRef]

32. Toyosaki, H.; Kawasaki, M.; Tokura, Y. Electrical properties of Ta-doped SnO$_2$ thin films epitaxially grown on TiO$_2$ substrate. *Appl. Phys. Lett.* **2008**, *93*, 132109. [CrossRef]

33. Nakao, S.; Yamada, N.; Hitosugi, T.; Hirose, Y.; Shimada, T.; Hasegawa, T. High Mobility Exceeding 80 cm^2 V^{-1}s^{-1} in Polycrystalline Ta-Doped SnO$_2$ Thin Films on Glass Using Anatase TiO$_2$ Seed Layers. *Appl. Phys. Express* **2010**, *3*, 031102. [CrossRef]

34. Weidner, M.; Jia, J.; Shigesato, Y.; Klein, A. Comparative study of sputter-deposited SnO$_2$ films doped with antimony or tantalum. *Phys. Stat. Sol* **2016**, *253*, 923–928. [CrossRef]

35. Muto, Y.; Oka, N.; Tsukamoto, N.; Iwabuchi, Y.; Kotsubo, H.; Shigesato, Y. High-rate deposition of Sb-doped SnO$_2$ films by reactive sputtering using the impedance control method. *Thin Soild Films* **2011**, *520*, 1178–1181. [CrossRef]

36. Jousse, D.; Constantino, C.; Chambouleyron, I. Highly Conductive and Transparent Amorphous Tin Oxide. *J. Appl. Phys.* **1983**, *54*, 431–434. [CrossRef]

37. Nomura, K.; Ohta, H.; Takagi, A.; Kamiya, T.; Hirano, M.; Hosono, H. Room-Temperature Fabrication of Transparent Flexible Thin-Film Transistors Using Amorphous Oxide Semiconductors. *Nature* **2004**, *432*, 488–492. [CrossRef] [PubMed]

38. Buchholz, D.B.; Ma, Q.; Alducin, D.; Ponce, A.; Jose-Yacaman, M.; Khanal, R.; Medvedeva, J.E.; Chang, R.P.H. The Structure and Properties of Amorphous Indium Oxide. *Chem. Mater.* **2014**, *26*, 5401–5411. [CrossRef]

39. Hu, S.; Lewis, N.S.; Ager, J.W.; Yang, J.; McKone, J.R.; Strandwitz, N.C. Thin-Film Materials for the Protection of Semiconducting Photoelectrodes in Solar-Fuel Generators. *J. Phys. Chem. C* **2015**, *115*, 24201–24228. [CrossRef]

40. Mayer, M. Ion Beam Analysis of Rough Thin Films. *Nucl. Instr. Meth. Phys. Res. B Nucl.* **2002**, *194*, 177–186. [CrossRef]

41. Bikowski, A.; Welzel, T.; Ellmer, K. The correlation between the radial distribution of high-energetic ions and the structural as well as electrical properties of magnetron sputtered ZnO:Al films. *J. Appl. Phys.* **2013**, *114*, 223716. [CrossRef]

42. Sigmund, P. Theory of Sputtering Yield of Amorphous and Polycrystalline Targets. *Phys. Rev.* **1969**, *184*, 383–416. [CrossRef]

43. Yeom, G.Y.; Kushner, M.J. Cylindrical Magnetron Discharges. I. Current-Voltage Characteristics for DC- and RF-Driven Discharge Sources. *J. Appl. Phys.* **1989**, *65*, 3816–3824. [CrossRef]

44. Ellmer, K. Magnetron Sputtering of Transparent Conductive Zinc Oxide: Relation between the Sputtering Parameters and the Electronic Properties. *J. Phys. D Appl. Phys.* **2000**, *33*, R17–R32. [CrossRef]

45. Ruscic, B.; Feller, D.; Peterson, K.A. Active Thermochemical Tables: Dissociation energies of several homonuclear first-row diatomics and related thermochemical values. *Theor. Chem. Acc.* **2014**, *133*, 1415. [CrossRef]

46. Kaufman, F. N_2O Bond Dissociation Energy. *J. Chem. Phys.* **1967**, *46*, 2449. [CrossRef]

47. Ellmer, K.; Cebulla, R.; Wendt, R. Characterization of a Magnetron Sputtering Discharge with Simultaneous RF-and DC-Excitation of the Plasma for the Deposition of Transparent and Conducting ZnO:Al-Films. *Surf. Coat. Techn.* **1998**, *98*, 1251–1256. [CrossRef]

48. Nomura, K.; Kamiya, T.; Ohta, H.; Ueda, K.; Hirano, M.; Hosono, H. Carrier Transport in Transparent Oxide Semiconductor with Intrinsic Structural Randomness Probed Using Single-Crystalline $InGaO_3(ZnO)_5$ Films. *Appl. Phys. Lett.* **2004**, *85*, 1993–1995.

49. Thienprasert, J.T.; Rujirawat, S.; Klysubun, W.; Duenow, J.N.; Coutts, T.J.; Zhang, S.B.; Look, D.C.; Limpijumnong, S. Compensation in Al-Doped ZnO by Al-Related Acceptor Complexes: Synchrotron X-Ray Absorption Spectroscopy and Theory. *Phys. Rev. Lett.* **2013**, *110*, 055502. [CrossRef]

50. Bikowski, A.; Zajac, D.A.; Vinnichenko, M.; Ellmer, K. Evidence for the AlZn-Oi defect-complex model for magnetron-sputtered aluminium-doped zinc oxide: A combined X-ray absorption near edge spectroscopy, X-ray diffraction and electronic transport study. *J. Appl. Phys.* **2019**, *126*, 045106. [CrossRef]

51. Tesmer, J.R.; Nastasi, M. (Eds.) *Handbook of Modern Ion Beam Materials Analysis*; MRS: Pittsburgh, PA, USA, 1995; p. 704.

52. Winters, H.F.; Kay, E. Gas Incorporation into Sputtered Films. *J. Appl. Phys.* **1967**, *38*, 3928–3934. [CrossRef]

53. Winters, H.F. Elementary Processes at Solid Surfaces Immersed in Low Pressure Plasmas. In *Plasma Chemistry III*; Veprek, S., Venugopalan, M., Eds.; Springer: Berlin/Heidelberg, Germany, 1980; Volume 94, pp. 69–125.

54. Lee, W.W.Y.; Oblas, D. Argon entrapment in metal films by dc triode sputtering. *J. Appl. Phys.* **1975**, *46*, 1728–1732. [CrossRef]

55. Thornton, J.A.; Hoffman, D.W. Internal Stresses in Amorphous Silicon Films Deposited by Cylindrical Magnetron Sputtering Using Ne, Ar, Kr, Xe, and $Ar+H_2$. *J. Vac. Sci. Techn.* **1981**, *18*, 203–207. [CrossRef]

56. Nie, M.; Bikowski, A.; Ellmer, K. Microstructure evolution of Al-doped zinc oxide and Sn-doped indium oxide deposited by radio-frequency magnetron sputtering: A comparison. *J. Appl. Phys.* **2015**, *117*, 155301. [CrossRef]

57. Minami, T.; Nanto, H.; Takata, S. Highly Conducting and Transparent SnO_2 Thin Films Prepared by RF Magnetron Sputtering on Low-Temperature Substrates. *Jap. J. Appl. Phys.* **1988**, *27*, L287–L289. [CrossRef]

58. Brousseau, J.-L.; Bourque, H.; Tessier, A.; Leblanc, R.M. Electrical properties and topography of SnO_2 thin films prepared by reactive sputtering. *Appl. Surf. Sci.* **1997**, *108*, 351–358. [CrossRef]

59. Fuchs, K. The conductivity of thin metallic films according to the electron theory of metals. *Proc. Cambridge Phil. Soc.* **1938**, *11*, 100–108. [CrossRef]

60. Sondheimer, E.H. The Mean Free Path of Electrons in Metals. *Adv. Phys.* **1952**, *1*, 1–42. [CrossRef]

61. Ellmer, K.; Mientus, R.; Weiß, V.; Rossner, H. In situ Energy-Dispersive X-Ray Diffraction System for Time-Resolved Thin Film Growth Studies. *Meas. Sci. Techn.* **2003**, *14*, 336–345. [CrossRef]

62. Kersten, H.; Deutsch, H.; Steffen, H.; Kroesen, G.M.W.; Hippler, R. The Energy Balance at Substrate Surfaces During Plasma Processing. *Vacuum* **2001**, *63*, 385–431. [CrossRef]

63. Weise, M.; Seeger, S.; Harbauer, K.; Welzel, T.; Ellmer, K. A multifunctional plasma and deposition sensor for the characterization of plasma sources for film deposition and etching. *J. Appl. Phys.* **2017**, *122*, 044503. [CrossRef]

64. Minami, T.; Oda, J.-I.; Nomoto, J.-I.; Miyata, T. Effect of Target Properties on Transparent Conducting Impurity-Doped ZnO Thin Films Deposited by DC Magnetron Sputtering. *Thin Solid Films* **2010**, *519*, 385–390. [CrossRef]

65. Kluth, O.; Schöpe, G.; Rech, B.; Menner, R.; Oertel, M.; Orgassa, K.; Schock, H.W. Comparative Material Study on RF and DC Magnetron Sputtered ZnO:Al Films. *Thin Solid Films* **2006**, *502*, 311–316. [CrossRef]

66. Szyszka, B. Magnetron Sputtering of ZnO Films. In *Transparent Conductive Zinc Oxide: Basics and Application in Thin Film Solar Cells*; Ellmer, K., Klein, A., Rech, B., Eds.; Springer: Berlin/Heidelberg, Germany, 2008; pp. 187–233.

67. Hotop, H.; Lineberger, W.C. Binding Energies in Atomic Negative Ions. *J. Phys. Chem. Ref. Data* **1975**, *4*, 539–576. [CrossRef]

68. Cuomo, J.J.; Gambino, R.J.; Harper, J.M.E.; Kuptsis, J.D. Origin and Effects of Negative Ions in the Sputtering of Intermetallic Compounds. *IBM J. Res. Dev.* **1977**, *21*, 580–583. [CrossRef]

69. Burstein, E. Anomalous Optical Absorption Limit in InSb. *Phys. Rev.* **1954**, *93*, 632–633. [CrossRef]

70. Moss, T.S. The Interpretation of the Properties of Indium Antimonide. *Proc. Phys. Soc. Sec. B* **1954**, *67*, 775–782. [CrossRef]